Key Points:

- The largest fluxes of $E = 2.0$ MeV electrons in GPS orbit were associated with *moderate* to *strong* CME-driven geomagnetic storms
- The majority of the 50 largest flux events at $L = 4.5$ (30 out of 50) and $L = 6.5$ (37 out of 50) were associated with high speed streams
- The 1 in 3 year flux levels at $L = 4.5$ and 6.5 were not exceeded following any of the 15 largest geomagnetic storms

Correspondence to:

N. P. Meredith,
nmer@bas.ac.uk

Strong Relativistic Electron Flux Events in GPS Orbit

Nigel P. Meredith[1] ⓘ, Thomas E. Cayton[2] ⓘ, Michael D. Cayton[2], and Richard B. Horne[1] ⓘ

[1]British Antarctic Survey, Natural Environment Research Council, Cambridge, England, [2]Rio Rancho, NM, USA

Abstract Relativistic electrons cause internal charging on satellites and are a significant space weather hazard. In this study we analyze approximately 20 years of data from the US Global Positioning System (GPS) satellite NS41 to determine the conditions associated with the largest daily averaged fluxes of $E = 2.0$ MeV relativistic electrons. The largest flux events at $L = 4.5$ and $L = 6.5$ were associated with *moderate* to *strong* CME-driven geomagnetic storms. However, the majority of the 50 largest flux events at $L = 4.5$ (30 out of 50) and $L = 6.5$ (37 out of 50) were associated with high speed solar wind streams from coronal holes. Both solar drivers are thus very important for relativistic electron flux enhancements in GPS orbit. The 1 in 3 year flux level was not exceeded following any of the 15 largest geomagnetic storms as monitored by the *Dst* index, showing that the largest geomagnetic storms, most often associated with extreme space weather, do not result in significantly larger relativistic electron flux events in GPS orbit.

Plain Language Summary Very high energy electrons can damage spacecraft and are a potential risk to humans in space. Here we use approximately 20 years of data from the US Global Positioning System (GPS) satellite NS41 to determine the conditions associated with the production of the largest numbers of these, so-called, "killer" electrons. The largest events in the outer radiation belt, a donut-shape zone of very high energy electrons encircling the Earth, were caused by large explosions from the Sun's outer atmosphere, known as coronal mass ejections. However, the majority of the 50 largest events were associated high speed streams of energetic electrons emanating from darker and cooler areas in the Sun's outer atmosphere, known as coronal holes. The largest events were associated with *moderate* to *strong* geomagnetic storms. In contrast, the largest geomagnetic storms, most often associated with extreme space weather, did not result in significantly larger high energy electron flux events in GPS orbit.

1. Introduction

Space weather, by definition, directly impacts both technological systems in orbit and those on Earth and is an important natural hazard risk. For example, during a severe space weather event satellites, GPS signals, high frequency radio communications, and power grids may all be affected (e.g., Royal Academy of Engineering Report, 2013). Our ever growing infrastructure is increasingly vulnerable to the potentially damaging effects of space weather.

The concern at government level in the UK is such that extreme space weather was added to the UK National Risk Register of Civil Emergencies in 2011 (Cabinet Office, 2012). The impact of a realistic worst case scenario for extreme space weather was recently raised from moderate to severe, putting it in the same impact/likelihood category as conventional attacks on infrastructure, low temperatures and snow, outbreak of a new and infectious diseases and nuclear miscalculation not involving the UK (Cabinet Office, 2023). The percentage chance of a realistic worst case scenario occurring in the next 5 years is currently estimated to be between 5 and 25% and the economic cost of such an event is estimated to be of the order of £ billions (Cabinet Office, 2023).

Relativistic electrons ($E > 0.5$ MeV) are a major source of radiation damage to satellites. These, so called "killer electrons", can penetrate satellite surfaces and embed themselves in insulating materials and ungrounded conductors. The charge can accumulate over time resulting in the build up of high electric fields in and between materials to breakdown levels (Frederickson et al., 1991; Rodgers & Ryden, 2001). The subsequent discharge can cause phantom commands, logic errors, erroneous data, loss of functionality and, in exceptional cases, serious harm to a satellite (e.g., Koons & Fennel, 2006).

Relativistic electrons in near Earth space tend to occupy two distinct regions referred to as the inner and outer radiation belt. The inner radiation belt, which typically occurs at altitudes between 640 and 6,400 km (geocentric distances between 1.1 and 2.0 Earth radii, R_E) in the Earth's magnetic equatorial plane, is relatively stable with

significant variations only occurring during the most intense geomagnetic storms (Baker et al., 2007). In contrast, the outer radiation belt, which typically occurs at altitudes between 13,000 and 45,000 km (geocentric distances between 3 and 8 R_E), is highly dynamic. In this region the fluxes of relativistic electrons may change by orders of magnitude on timescales ranging from minutes to weeks (e.g., Baker et al., 1994; Blake et al., 1992). This variability is controlled by a variety of transport, acceleration and loss mechanisms (e.g., Horne et al., 2005; Li & Hudson, 2019; Shprits, Elkington, et al., 2008; Shprits, Subbotin, et al., 2008; Thorne, 2010, 2013), all of which become enhanced during enhanced geomagnetic activity, which is ultimately driven by the Sun.

Satellites, including Earth observation, communication and global navigation satellites are now recognised as critical infrastructure (e.g., Cabinet Office (2018)). This infrastructure extends out to 6.6 Earth radii, including the regions occupied by the inner radiation belt and the vast majority of the outer radiation belt. As of 1 May 2023 there were over 7,500 operational satellites in Earth orbit including 6,768 in low Earth orbit, 143 in medium Earth orbit and 590 in geostationary orbit (https://www.ucsusa.org/resources/satellite-database). Most are exposed to relativistic electrons in the Earth's radiation belts at some or all points in their orbits.

There are two principle solar drivers of geomagnetic storms: coronal mass ejections (CMEs) and coronal holes (e.g., Gonzalez et al., 1999). CMEs are large explosions on the Sun that hurl vast amounts of magnetized plasma into space, leading to episodic storms that peak during solar maximum (St. Cyr et al., 2000). They are associated with a broad range of propagation speeds, ranging from 250 to 950 kms^{-1} (Gopalswamy & Kundu, 1992; Kilpua et al., 2017). The largest geomagnetic storms, as monitored by the *Dst* index, are driven by interplanetary coronal mass ejections, the interplanetary counterpart of CMEs. Such storms typically have minimum *Dst* indices of less than −100 nT and are associated with recovery phases of the order of a couple of days.

Coronal holes are large dark areas on the Sun as seen in extreme ultraviolet (EUV) and soft X-ray images (Cranmer, 2009). They are regions of open magnetic field and cooler plasma, leading to the production of high-speed solar wind streams (HSSs). A HSS is characterized by an enhancement in the solar wind velocity lasting for several days. Typically, the speed exceeds 500 kms^{-1} for 2–3 days and may reach a maximum above 800 kms^{-1} (e.g., Denton & Borovsky, 2012). Coronal holes are long-lasting features that can persist from one solar rotation to the next, giving rise to a 27 day periodicity in the arrival of HSSs at Earth. The occurrence rate of coronal holes peaks during the declining phase of the solar cycle (Burlaga & Lepping, 1977; Gonzalez et al., 1999). HSS-driven storms are predominantly responsible for *weak* to *moderate* geomagnetic storms (e.g., Tsurutani et al., 1995) with an average minimum *Dst* index of −40 nT (Richardson et al., 2006). However, they have much more extensive recovery phases, typically lasting from 5 to 10 days, and, as a result, may deposit more energy in the magnetosphere than larger CME-driven storms (Kozyra et al., 2006; Turner et al., 2006).

Global Navigation Satellite System (GNSS) satellites such as the US GPS satellites and the European Galileo navigation system operate in Medium Earth Orbit (MEO) at altitudes between 19,000 and 24,000 km. GNSS enabled devices are used all over the world for navigation, positioning, tracking, mapping and timing. It is, therefore, important to have a comprehensive understanding of the environment encountered by satellites in GNSS-type orbits and, in particular, knowledge of the conditions associated with extremes of this environment. For example, Gabrielse et al. (2022) built a model of radiation belt fluxes (RB-Daily-E) to visualize the fluences at GPS satellites from 2012 to 2019, finding fluences spiked during years of increased geomagnetic storms, and that fluence rate of change corresponded with the satellite's solar array voltage degradation rate of change.

The largest relativistic electron fluxes encountered between December 2000 and July 2020 in GPS orbit occurred during the *moderate* geomagnetic storm, of 6 April 2010. This storm was driven by a modest CME at the leading edge of a magnetized high-speed stream, with a minimum *Dst* index of −81 nT (Meredith et al., 2023). In contrast, one of the largest storms in the last 25 years, the so-called Halloween storm in 2003, was not associated with large fluxes of relativistic electrons either at $L = 4.5$ or at $L = 6.5$ on field lines mapping to geosynchronous orbit (Meredith et al., 2023). Indeed, during this *great* storm, according to the classification scheme proposed by Loewe and Prolls (1997), a new radiation belt formed at low L, peaking in the slot region (Baker et al., 2004).

These results have led to suggestions that satellites in GPS and geosynchronous orbit could be more at risk during a milder solar storm than from an extreme storm (Meredith et al., 2023; Pultarova, 2023). This is an interesting suggestion, but it is only based on two events. In this study we use approximately 20 years of data from the US GPS satellite NS41 to conduct a survey of the 50 largest relativistic electron flux events. In particular, we examine the data at $L = 4.5$ near the heart of the outer radiation belt and at $L = 6.5$, on field lies that map to geosynchronous

orbit respectively, to investigate the type and strength of the geomagnetic storms responsible for significant relativistic electron flux enhancements in these two important regions. The instrumentation and data analysis are first described in Section 2. Case studies showing two different responses are shown in Section 3 and the results of the full survey are presented in Section 4. Finally, the results are discussed and the conclusions presented in Sections 5 and 6 respectively.

2. Instrumentation and Data Analysis

2.1. Instrumentation

The data used in this study were collected by the Burst Detector Dosimeter IIR (BDD-IIR) on board the US GPS satellite NS41. NS41 was launched on 10 November 2000 and operated in a circular orbit at an altitude of 20,200 km with an inclination of 55° and a period of 12 hr. It crossed the magnetic equator around $L = 4.2$ and sampled higher L shells at higher magnetic latitudes. For this study we use data from the entire mission, extending from 10 December 2000–25 July 2020.

BDD-IIR is a multi purpose silicon detector system. It features eight individual channels of a "shield/filter/sensor" design that permits the detector to sample roughly half the celestial sphere while at the same time shielding the silicon sensor elements from most of the incident particle flux. Absorbers in front of the sensors determine the energy thresholds for measuring the incident particle fluxes. The aperture dimensions were chosen in an attempt to achieve equal counting rates in all channels. During on-orbit operation none of the BDD-IIR's channels appeared to saturate. Background counting rates were found to be well behaved. For each week of data, mean values of the counting rates of the 8 channels were compiled from accumulations reported from L values larger than 20. Here L is the McIlwain L value calculated using the IGRF internal field and the Olson-Pfitzer quiet-time external field (Olson & Pfitzer, 1977). Except for weeks with one or more solar energetic particle (SEP) events, the weekly mean values were used for the background counting rates for each of the 2520 individual records. During SEPs, the background estimation followed the evolution of the SEP and were time dependent.

The deposited energy thresholds were calibrated carefully (Cayton et al., 1998). Electron response functions for the channels were determined by detailed modeling of the instrument by Monte Carlo methods (Tuszewski et al., 2002). The electron response functions are most sensitive to the highest energy incident electrons. Any electron spectrum covering the energy range from 0.1 to 10 MeV can be folded with the response functions to predict counting rates in all eight channels due to that spectrum. Adding background counting rates to these yields a set of model counting rate that may be compared directly with the measured rates (corrected for the measured 6 ms dead-time). Best-fitting relativistic-Maxwellian spectra were determined by minimizing the sum of squared differences of a set of model counting rates (background plus ones due the spectrum of electrons) and the set of dead-time corrected measured counting rates. Each of the best-fitting spectra covers the energy range 0.1–10 MeV. Commonly observed spectral features (i.e., remarkably exponential shapes) of relativistic electrons in the outer radiation belt (Cayton et al., 1989; Pierrard & Lemaire, 1996; Reagan et al., 1981) provided guidance for the selection of the relativistic Maxwellian as the functional form for these model spectra.

For incident energies above 0.5 MeV, electron fluxes evaluated from a single Maxwellian component well represent observed fluxes; however, below 0.5 MeV, the single-component model systematically underestimates the actual flux, because an additional lower-energy component dominates at the lower energies. We focus on relativistic electrons with energies of 2.0 MeV, well above the 0.5 MeV threshold below which the single component fits do not perform so well. We note that on the lowest L-shells visited by GPS orbit, electron spectra during periods of decay exhibit characteristic non-equilibrium leakage features (Duderstadt & Hamilton, 1976). These particular features, however, are not associated with electron enhancements that follow large magnetic storms, and, thus, are not expected to significantly affect our results.

Data from BDD-IIR have been extensively used in the DREAM model (Koller et al., 2007; Reeves et al., 2012), to calculate expected solar array degradation (Messenger et al., 2011) to characterize relativistic electron flux rise times (Varotsou et al., 2008) and to estimate the worst case relativistic electron spectra in GPS orbit (Meredith et al., 2023).

For additional details regarding the BDD-IIR instrument, its calibration, numerical modeling, and limitations, see Cayton et al. (2004), and Meredith et al. (2023).

2.2. Data Analysis

The NS41 BDD-IIR data used in this study were downloaded from the United States Department of Commerce's National Oceanic and Atmospheric Administration (NOAA) website. Each normal file includes 2520 records of duration 240 s, corresponding to one GPS-week of data. Each weekly file was examined, and excess records (almost always containing only "fill" values) were eliminated. Of the total of 1024 GPS-weeks during the lifetime of the mission, 31 were missing entirely, 3 included data for one day and 1 included data for two days. We used the data from the remaining 989 full weekly files in this study.

Electron differential fluxes at 10 energies (0.6, 0.8, 1.0, 1.6, 2.0, 3.0, 4.0, 5.0, 6.0 and 8.0 MeV) were written into separate files for each crossing of 12 equally spaced L-shells between $L = 4.25$ and $L = 7.00$ (Meredith et al., 2023). NS41 crosses each of the specified L-shells as many as 8 times each day. The differential fluxes were then plotted as a function of time for each energy and L value to verify the absence of outliers and other anomalies in the data. Daily averaged fluxes were then compiled for each of the specified L-shells. For additional details regarding the data processing for BDD-IIR, see Meredith et al. (2023).

3. Case Studies

3.1. Largest Event

The largest daily average fluxes of $E = 2.0$ MeV electrons encountered during the entire mission were observed during the 6 April 2010 geomagnetic storm. This was a *moderate* geomagnetic storm with a minimum *Dst* index of −81 nT on 6 April.

Figure 1 shows the flux of $E = 2.0$ MeV electrons as a function of time for selected values of L in April 2010. Individual measurements are coded blue and the daily averages, used in the analysis, are coded black. To put the data into context the figure also shows relevant geophysical indices and solar wind parameters. Figure 1 shows (a–f) the $E = 2.0$ MeV electron flux at $L = 7.0, 6.5, 6.0, 5.5, 5.0,$ and 4.5, respectively; (g) the solar wind speed (red trace) and the Interplanetary Magnetic Field (IMF) Bz (black trace); (h) the *Dst* index (color coded) and solar wind pressure (black trace); and (i) the Kp (color coded) and AE (black trace) indices. The dotted line in each of the panels a–f denotes the daily average flux value which is exceeded in 1% of the daily averaged flux values at each L, taken over the entire mission. Henceforth, we refer to this value as the 1% exceedance level.

The 1% exceedance level is surpassed for several days at each L value, with the peak values of $E = 2.0$ MeV electrons being the largest fluxes at that L value observed during the entire mission (Table 1). The table also includes the theoretical 1 in 10 and 1 in 100 year flux levels as determined from an extreme value analysis of the NS41 BDD-IIR data (Meredith et al., 2023). The highest fluxes were observed at $L = 4.5$ and 5.0 on 8 April 2010 and are very close to the theoretical 1 in 100 year fluxes. Further out, in the region $5.5 < L < 7.0$ the largest fluxes were seen two days later on 10 April 2010 and also approach the 1 in 100 year flux levels.

These large fluxes are associated with several days of enhanced geomagnetic activity followed by a *moderate* geomagnetic storm that began on 5 April 2010.

3.2. Largest Geomagnetic Storm

The largest geomagnetic storm of the entire mission, with a minimum *Dst* index of −422 nT, occurred on 20 November 2003. The measured fluxes and daily average fluxes for this month are plotted in Figure 2, in the same format as Figure 1. This storm was not associated with the production of large fluxes of relativistic electrons in GPS orbit. In fact, the daily average fluxes of $E = 2.0$ MeV electrons remained below the 1% exceedance level at all L shells in the region $4.5 < L < 7$. Interestingly, the post-storm fluxes were less than the pre-storm fluxes in the region $4.5 < L < 6.5$.

At $L = 4.5$ the fluxes peaked at $2.41 \times 10^5 \text{ cm}^{-2}\text{s}^{-1}\text{sr}^{-1}\text{MeV}^{-1}$, 6 days after the Dst minimum, a factor of 8.2 less than the largest flux associated with the 6 April 2010 storm in this region. Further out, at $L = 6.5$, the fluxes peaked at $1.26 \times 10^4 \text{ cm}^{-2}\text{s}^{-1}\text{sr}^{-1}\text{MeV}^{-1}$, 7 days after the Dst minimum, a factor of 6.6 less than the largest flux associated with the 6 April 2010 storm.

These results suggests that modest storms may pose more of a risk to satellites in GPS orbit than the largest storms that are more typically associated with extreme space weather.

Figure 1. Summary plot of the NS41 Burst Detector Dosimeter IIR E = 2.0 MeV electron flux for April 2010 (a–f) at L = 7.0, 6.5, 6.0, 5.5, 5.0, and 4.5, respectively; (g) the solar wind speed (red trace) and Interplanetary Magnetic Field Bz (black trace); (h) the Dst index (color coded) and solar wind pressure (black trace); and (i) the Kp (color coded) and AE (black trace) indices. The dotted lines in panels a–f represent the 1% exceedance level at each value of L.

Table 1
Largest Daily Averaged Fluxes of E = 2.0 MeV Electrons Observed in GPS Orbit Between 10 December 2000 and 25 July 2020 as a Function of L and the Corresponding 1 in 10 and 1 in 100 Year Flux Levels

L	Date	Largest flux ($cm^{-2}s^{-1}sr^{-1}MeV^{-1}$)	1 in 10 year flux ($cm^{-2}s^{-1}sr^{-1}MeV^{-1}$)	1 in 100 year flux ($cm^{-2}s^{-1}sr^{-1}MeV^{-1}$)
4.5	8 April 2010	1.98×10^6	1.77×10^6	2.04×10^6
5.0	8 April 2010	9.77×10^5	7.60×10^5	9.88×10^5
5.5	10 April 2010	4.31×10^5	3.31×10^5	4.79×10^5
6.0	10 April 2010	2.50×10^5	1.69×10^5	2.73×10^5
6.5	10 April 2010	1.45×10^5	9.18×10^4	1.63×10^5
7.0	10 April 2010	8.26×10^4	4.97×10^4	1.12×10^5

To examine this finding in more detail we looked at the storm strengths and solar drivers associated with the 50 largest $E = 2.0$ MeV flux events at $L = 4.5$ and 6.5. We then compared the results with the peak $E = 2.0$ MeV fluxes associated with the 15 strongest geomagnetic storms.

4. Geomagnetic Storm Study

For our geomagnetic storm study, we first identified the 50 largest, independent, $E = 2.0$ MeV relativistic electron flux events throughout the mission at $L = 4.5$ and $L = 6.5$. For each event we examined the behavior of the relativistic electron fluxes, the geomagnetic indices and the solar wind parameters over the preceeding 10 days to identify the driver and strength of the associated geomagnetic storm. We noted the minimum in the *Dst* index and the storm type. CME-driven storms were confirmed using the Richardson and Cain list of near-Earth interplanetary coronal mass ejections (Richardson & Cane, 2024) and high speed streams confirmed using the SIR/HSS event catalog presented in Grandin et al. (2019).

For each event, we classified the storm strength by the minimum value of the *Dst* index associated with the storm, as defined by Loewe and Prolls (1997) and tabulated in Table 2. Here, and elsewhere, we use the five italicized terms *weak*, *moderate*, *strong*, *severe*, and *great* to signify the storm categories as defined in Table 2.

We also determined the characteristic width of each event, which we estimated by computing the full width at half maximum (FWHM), defined, for each event as the time during which the daily averaged flux remained greater than half of the maximum flux associated with the event. On three occasions, marked by asterisks in Table A1, the flux remained larger than the half maximum value but did undergo a local minimum. For these three cases we used the local minimum to define the characteristic width.

4.1. L = 4.5

The 50 largest $E = 2.0$ MeV electron flux events at $L = 4.5$ are shown as a function of storm strength, as monitored by the minimum in the *Dst* index, in Figure 3 and tabulated in Table A1. Events associated with CMEs are coded red and those associated with high speed solar wind streams are coded orange. The 1 in 2, 1 in 10 and 1 in 100 year fluxes of $E = 2.0$ MeV electrons at $L = 4.5$ are denoted by the dashed, dot-dashed, and solid purple lines respectively.

The majority of the largest $E = 2.0$ MeV electron flux events at $L = 4.5$, near the usual position of the heart of the outer radiation belt, were associated with either *moderate* (33 out of 50) or *strong* (11 out of 50) geomagnetic storms. Of the remainder, three were associated with *weak* storms, two with *severe* storms and one with a *great* storm.

The majority of the larger storms associated with the 50 largest events were driven by CMEs. For example, all but three of the storms (19 out of 22) with a *Dst* minimum less than −80 nT were driven by CMEs, consistent with previous surveys which have found that CME's are more effective at producing larger storms than high speed streams (e.g., Yermolaev and Yermolaev (2002); Denton et al. (2006)). In sharp contrast, the majority of the smaller storms were driven by high speed streams, with all bar one of the storms (27 out of 28) with a *Dst* minimum greater than −80 nT being driven by high speed streams.
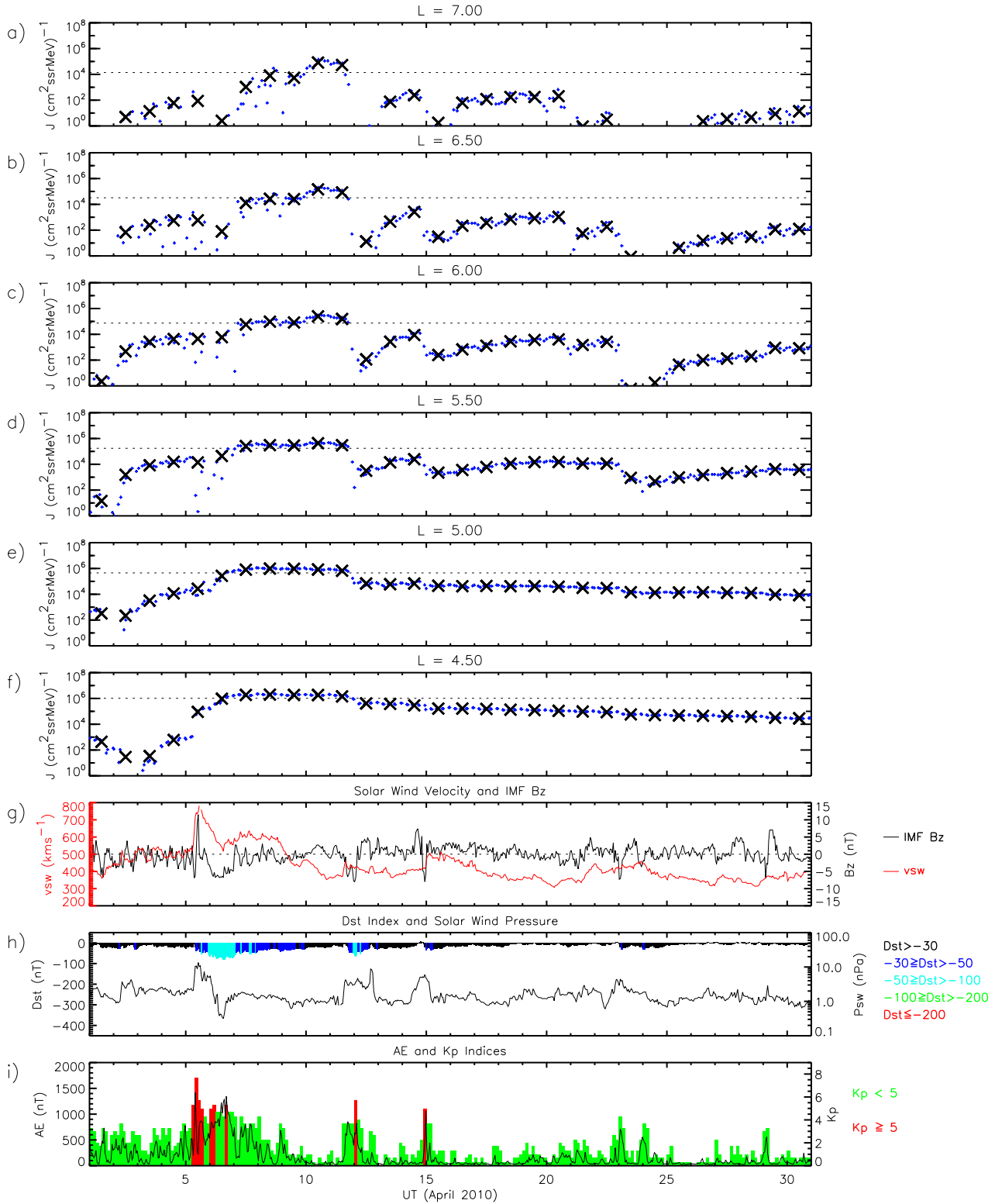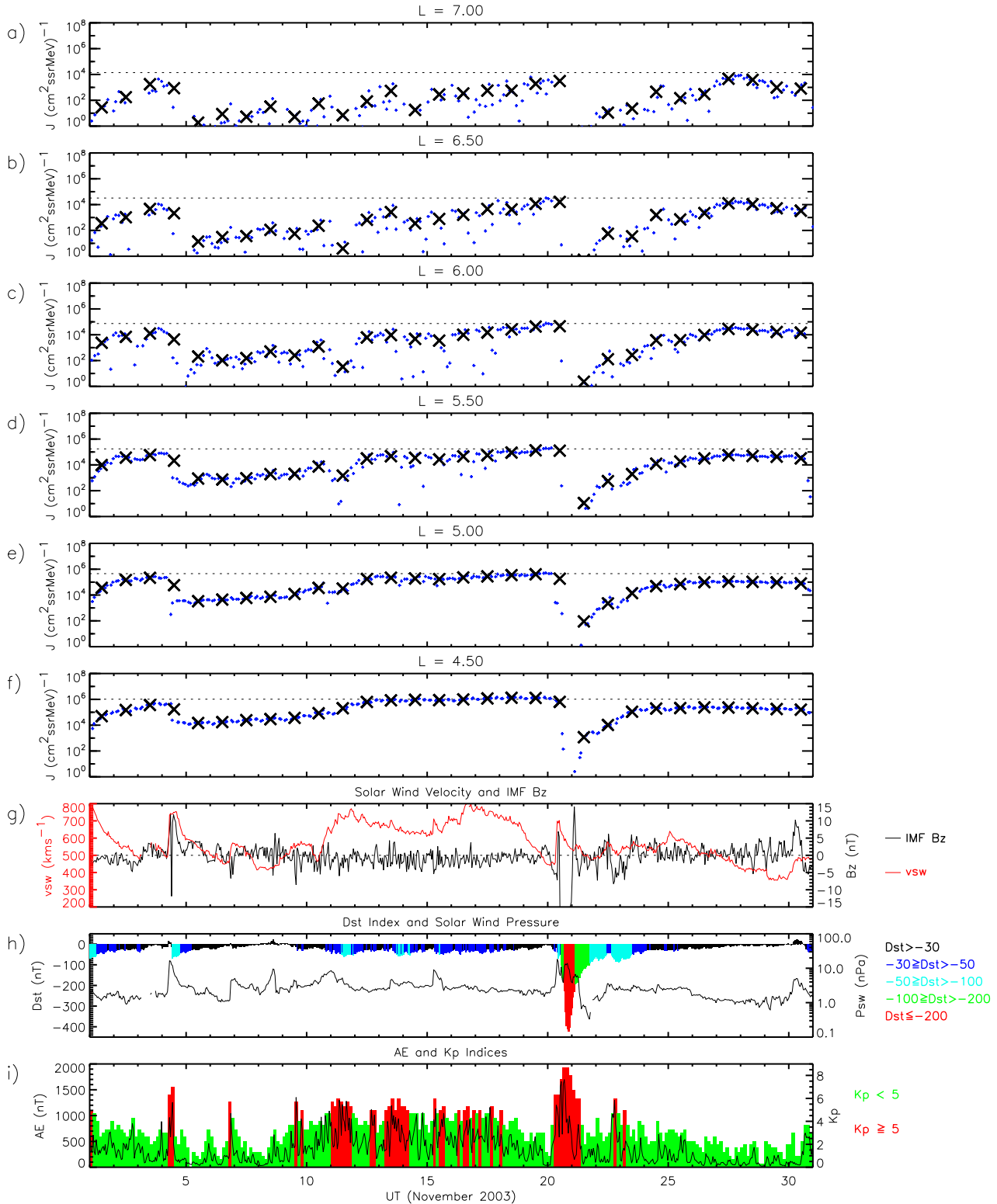
Figure 2. Summary plot of the NS41 Burst Detector Dosimeter IIR E = 2.0 MeV electron flux for November 2003 (a–f) at L = 7.0, 6.5, 6.0, 5.5, 5.0, and 4.5, respectively; (g) the solar wind speed (red trace) and Interplanetary Magnetic Field Bz (black trace); (h) the Dst index (color coded) and solar wind pressure (black trace); and (i) the Kp (color coded) and AE (black trace) indices. The dotted lines in panels a–f represent the 1% exceedance level at each value of L.

Table 2
Storm Categories

Storm strength	Dst range
weak	$-30 > Dst_{min} > -50$ nT
moderate	$-50 > Dst_{min} > -100$ nT
strong	$-100 > Dst_{min} > -200$ nT
severe	$-200 > Dst_{min} > -350$ nT
great	$Dst_{min} < -350$ nT

Looking at the largest fluxes observed during the entire mission, the 1 in 2 year daily average flux of $E = 2.0$ MeV electrons was exceeded on seven occasions. These flux enhancements were mostly associated with *moderate* (4) and *strong* (2) storms, five being associated with CMEs and one being associated with a high speed solar wind stream, showing the largest flux enhancements at $L = 4.5$ tend to be associated with *moderate* or *strong* CME-driven storms. One of these events was associated with a *severe* storm driven by a CME, showing that *severe* storms can cause significant enhancements at $L = 4.5$ but are not a requirement for a significant flux enhancement in this region. Looking at the more extreme events, the 1 in 10 year daily average flux of $E = 2.0$ MeV electrons was exceeded on three occasions. These events were associated with *moderate* or *strong* CME-driven storms.

The peak daily average $E = 2.0$ MeV electron fluxes associated with the strongest 15 storms as monitored by the *Dst* index are plotted in Figure 4 and tabulated in Table C1. As in Figure 3, the 1 in 2, 1 in 10 and 1 in 100 year fluxes of $E = 2.0$ MeV electrons are denoted by the dashed, dot-dashed, and solid purple lines respectively. However, the *y*-axis scale is different, being logarithmic rather than linear, due to the much larger range of the peak fluxes associated with the largest storms. This storm subset includes 6 *strong* storms, 5 *severe* storms and 4 *great* storms. Three of these events resulted in fluxes of $E = 2.0$ MeV near the 1 in 2 year level, with the largest event having a flux of 1.45×10^6 cm^{-2}s^{-1}sr^{-1}MeV^{-1}, equating to a 1 in 2.6 year event. The peak fluxes associated with the remaining 12 storms were all a factor of four or more less than the 1 in 2 year flux. None approached the 1 in 10 or 1 in 100 year level. In particular, the largest flux associated with a great storm, 1.25×10^6 cm^{-2}s^{-1}sr^{-1}MeV^{-1}, equates to a 1 in 1.5 year event; the peak fluxes associated with the other 3 great storms being smaller by factors of 3.44, 5.19, and 5.36.

The 50 largest $E = 2.0$ MeV electron flux events are shown as a function of time in Figure 5a, together with the sunspot number in Figure 5b. The 1 in 2, 1 in 10 and 1 in 100 year fluxes of $E = 2.0$ MeV electrons are denoted by the dashed, dot-dashed, and solid purple lines respectively. There are two clear data clusters, with 24 of the events occurring between 2003 and 2007 inclusive, during the declining phase of solar cycle 23 (Sawadogo et al., 2024), and 19 events occurring between 2015 and 2018 inclusive, during the declining phase of solar cycle 24 (Sawadogo et al., 2024). The largest observed flux of $E = 2.0$ MeV electrons during the entire mission occurred shortly after solar minimum. Six other events exceeded the 1 in 2 year level and these were all observed during the declining phase of solar cycle 23. None of the events during the declining phase of solar cycle 24 exceeded the 1 in 2 year level.

A histogram showing the distribution of the characteristic widths of the 50 largest $E = 2.0$ MeV flux events is displayed as the red trace in Figure 6. The FWHM, on the *x* axis, is measured in days, and the number of events in
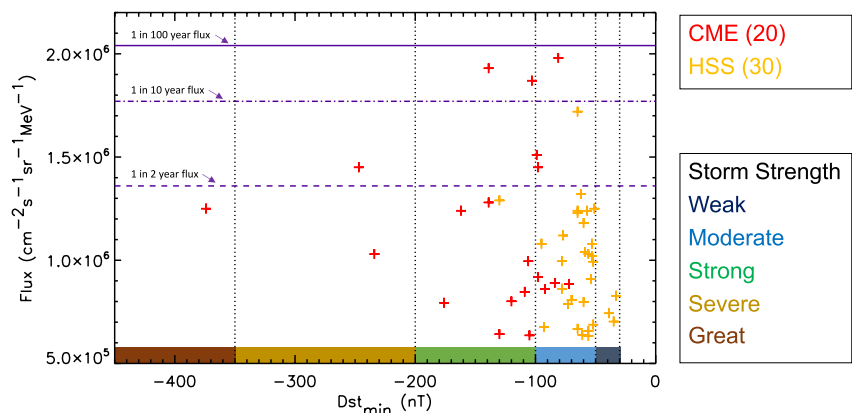

Figure 3. The 50 largest $E = 2.0$ MeV daily average electron flux events as a function of storm strength as monitored bye the *Dst* index. CME-driven storms are coded red and high speed stream driven storms are coded orange. The dashed, dot-dashed, and solid purple lines represent the 1 in 2, 1 in 10 and 1 in 100 year flux levels respectively.
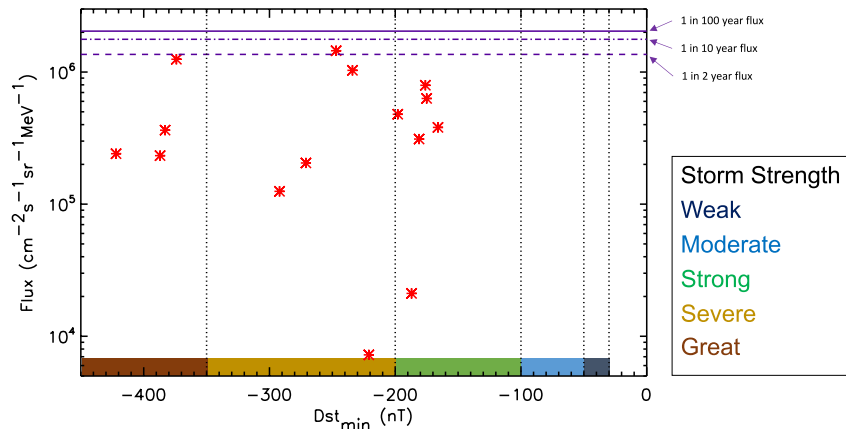
Figure 4. The maximum $E = 2.0$ MeV daily average electron fluxes at $L = 4.5$ associated with the largest 15 storms as monitored by the Dst index. The dashed, dot-dashed, and solid purple lines represent the 1 in 2, 1 in 10 and 1 in 100 year flux levels respectively.

each category are plotted on the y axis. The characteristic widths associated with the top fifty $E = 2.0$ MeV events at $L = 4.5$ range from 2.8 to 15.3 days with a mean characteristic width of 7.9 ± 2.5 days.

4.2. $L = 6.5$

The 50 largest $E = 2.0$ MeV electron flux events at $L = 6.5$, on field lines that map to the vicinity of geosynchronous orbit, are shown as a function of storm strength in Figure 7, in the same format as Figure 3, and tabulated in Table B1.

We note that the flux near the magnetic equator at $L = 6.5$ could be higher if the equatorial pitch angle distribution is peaked near 90° as electrons mirroring near the equator are not sampled at higher magnetic latitudes. Specifically, NS41 typically crossed $L = 6.5$ at magnetic latitudes between 35–38°. Here, assuming a dipole field, mirroring
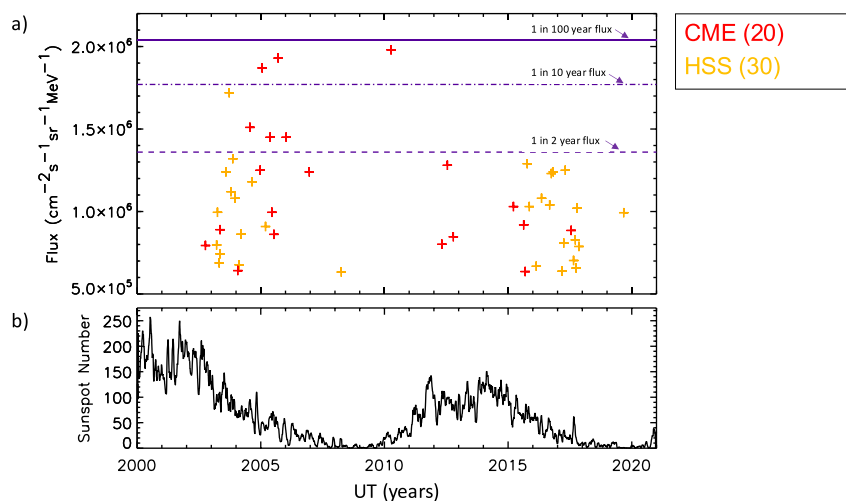

Figure 5. (a) The 50 largest $E = 2.0$ MeV daily average electron flux events at $L = 4.5$ as a function of time. The dashed, dot-dashed, and solid purple lines represent the 1 in 2, 1 in 10 and 1 in 100 year flux levels respectively; (b) the 27 days average sunspot number as a function of time.

Histograms of the Distributions of the Characteristic Widths
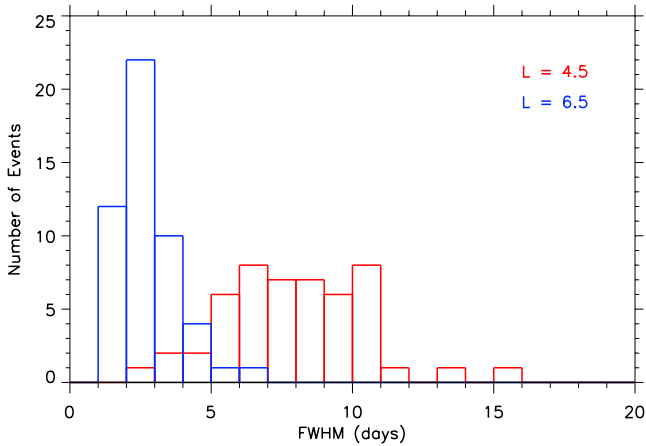of the Fifty Largest Flux Enhancements at L = 4.5 and L = 6.5

Figure 6. The distribution of the full width half maxima (FWHM) for the 50 largest flux events at $L = 4.5$ (red trace) and $L = 6.5$ (blue trace). The FWHM, on the x axis, is measured in days and the number of events are plotted on the y axis.

electrons would have equatorial pitch angles between 24 and 28°. Larger pitch angles would not be sampled. Shi et al. (2016) recently reported relatively flat relativistic electron pitch angle distributions in the outer radiation belt, both during quiet and active conditions, typically being represented by $\sin^n(\alpha)$ distribution with n less than 1. This implies that the pitch angle distributions will be relatively flat and that the omnidirectional flux measured at the equator could be similar to or a factor of 2 or 3 larger than those measured in GPS orbit, depending on the anisotropy. However, since we do not know the anisotropy for the specific events, we do not attempt a flux conversion and, in this section, focus on the results at $L = 6.5$ in GPS orbit.

The majority of the largest flux events at $L = 6.5$ were associated with either *weak* (12 out of 50) or *moderate* (30 out of 50) storms. Of the remainder, five were associated with *strong* storms, one was associated with a *severe* storm, one was associated with a *great* storm and one fell into a category below the definition of a *weak* storm.

Looking at the solar drivers, the majority of the largest flux events at $L = 6.5$ (37 out of 50) were associated with high speed streams and the remainder (13 out of 50) with CMEs. There is strong tendency for the larger storms to be associated with CMEs and the weaker storms to be associated with high speed streams with 12 out of 15 storms with a *Dst* minimum less than or equal to −80 nT being driven by CMEs and 34 out of 35 storms with a *Dst* minimum greater than −80 nT being driven by high speed streams.

Looking at the largest fluxes observed during the entire mission, the 1 in 2 year daily average flux of $E = 2.0$ MeV electrons was exceeded on seven occasions. These flux enhancements were associated with *moderate* (5) and *strong* (2) storms, four being associated with high speed streams and three being associated with CMEs. None of these events were associated with *severe* or *great* storms. Looking at the more extreme events, the 1 in 10 year daily average flux of $E = 2.0$ MeV electrons was exceeded on two occasions, one associated with a *moderate* and the other with a *strong* CME-driven storm.

The peak daily average $E = 2.0$ MeV electron fluxes associated with the strongest 15 storms as monitored by the *Dst* index are plotted in Figure 8 and tabulated in Table C1. Three of these events resulted in fluxes of $E = 2.0$ MeV near the 1 in 2 year level, with the largest event having a flux of 6.02×10^4 cm^{-2}s^{-1}sr^{-1}MeV^{-1}, equating to a 1 in 2.5 year event. The peak fluxes associated with the remaining 12 storms were all a factor of 3 or

The Fifty Largest E = 2.0 MeV Electron Flux Events at L = 6.5
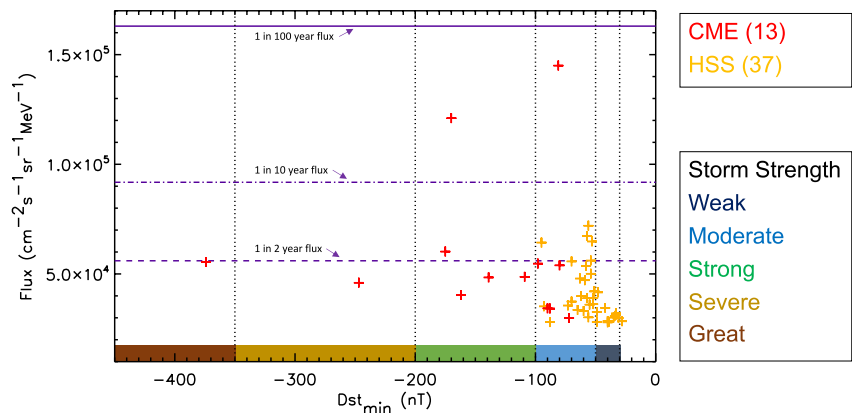
Figure 7. The 50 largest $E = 2.0$ MeV daily average electron flux events at $L = 6.5$ as a function of storm strength as monitored by the *Dst* index. CME-driven storms are coded red and high speed stream driven storms are coded orange. The dashed, dot-dashed, and solid purple lines represent the 1 in 2, 1 in 10 and 1 in 100 year flux levels respectively.
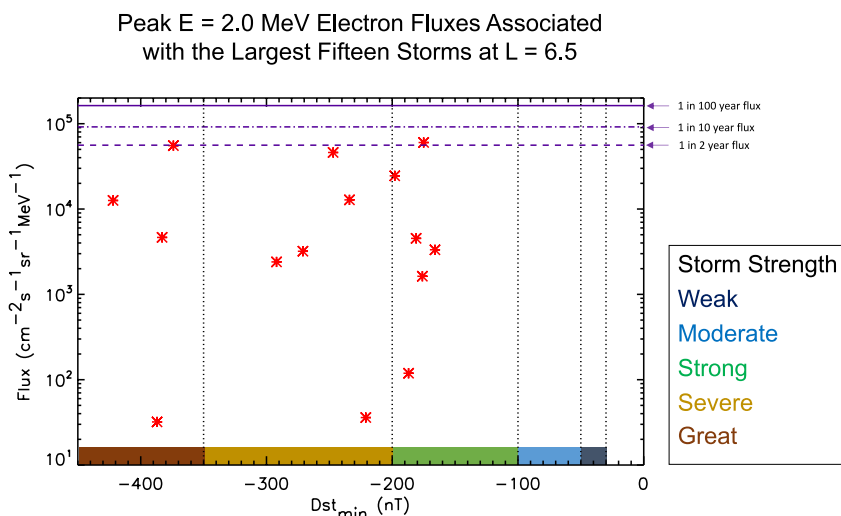
Figure 8. The maximum $E = 2.0$ MeV daily average electron fluxes at $L = 6.5$ associated with the largest 15 storms as monitored by the Dst index. The dashed, dot-dashed, and solid purple lines represent the 1 in 2, 1 in 10 and 1 in 100 year flux levels respectively.

more less than the 1 in 2 year flux. None approached the 1 in 10 or 1 in 100 year level. In particular, the largest flux associated with a great storm, 5.53×10^4 cm^{-2}s^{-1}sr^{-1}MeV^{-1} equates to a 1 in 2 year event; the peak fluxes associated with the other 3 great storms being smaller by factors of 4.39, 11.9, and 1,730.

The 50 largest $E = 2.0$ MeV electron flux events are shown as a function of time in Figure 9a, together with the sunspot number in Figure 9b. Again, there are two clear data clusters, with 27 of the events occurring during the declining phase of solar cycle 23 and 12 events occurring during the declining phase of solar cycle 24. The largest observed flux of $E = 2.0$ MeV electrons during the entire mission occurred shortly after solar minimum. Six other events exceeded the 1 in 2 year level, two during the declining phase of solar cycle 23, one during the solar minimum and three during the declining phase of solar cycle 24.

Figure 9. (a) The 50 largest $E = 2.0$ MeV daily average electron flux events at $L = 6.5$ as a function of time. The dashed, dot-dashed, and solid purple lines represent the 1 in 2, 1 in 10 and 1 in 100 year flux levels respectively; (b) the 27 days average sunspot number as a function of time.
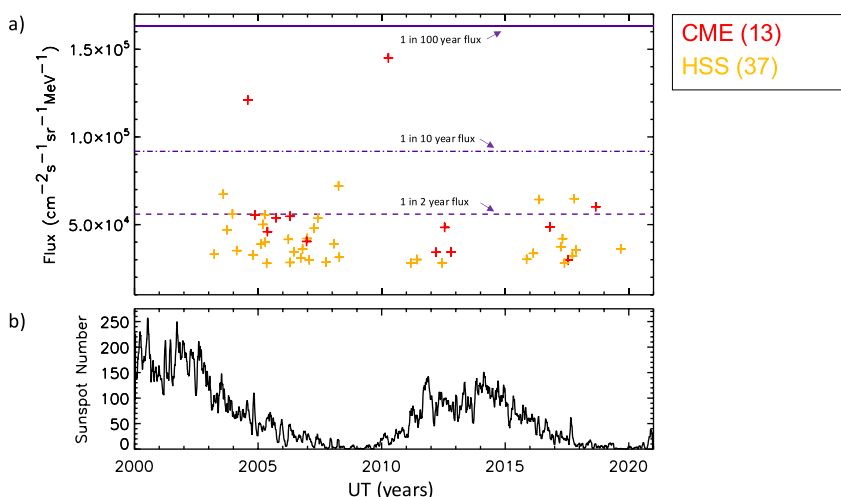
A histogram showing the distribution of the characteristic widths of these events is displayed as the blue trace in Figure 6. The characteristic widths of the flux enhancements associated with the top fifty $E = 2.0$ MeV events at $L = 6.5$ range from 1.6 to 6.5 days with a mean characteristic width of 2.8 ± 1.0 days.

5. Discussion

The largest $E = 2.0$ MeV electron fluxes observed during the mission occurred following the 6 April 2010 geomagnetic storm. This was a somewhat remarkable event in that it occurred close to solar minimum, following the so-called "electron desert" when the fluxes of $E = 2.0$ MeV electrons at $L = 4.5$ remained a factor of 100 below the 1% exceedance level for over 16 months. It also came as a surprise to satellite operators, engineers and insurers, who, based on the recent data, would not have been expecting such a large relativistic electron flux event.

The 6 April 2010 geomagnetic storm, associated with the largest fluxes of $E = 2.0$ MeV electron fluxes observed during the mission, was a relatively modest CME-driven storm with a minimum *Dst* index of -81 nT. However, the solar wind speed was high, remaining over 500 kms^{-1} from 5 to 9 April and the IMF Bz was predominantly southward. These solar wind conditions drove some extended and enhanced geomagnetic activity as monitored by the *AE* and *Kp* indices. Such periods are known to be associated with prolonged substorm activity, enhanced levels of seed electrons and chorus wave activity (Li et al., 2009; Meredith et al., 2001, 2020) and the gradual acceleration of electrons to relativistic energies (e.g., Jaynes et al., 2015; Meredith et al., 2003).

The largest fluxes of $E = 2.0$ MeV electrons in GPS orbit tend to be observed during the declining phase of the solar cycle. Interestingly, this is true for both the CME and HSS driven events. This result is unexpected for CME-driven storms, which peak during solar maximum (St Cyr et al., 2000), suggesting that there might be something about the declining phase that enables CME-driven storms to produce higher fluxes of relativistic electrons. The strength of the solar cycle is also important and the responses can be different from one cycle to the next. For example, at $L = 4.5$, the 1 in 2 year flux of $E = 2.0$ MeV electrons was exceeded six times during the declining phase of solar cycle 23 but was not exceeded at all during the declining phase of the weaker solar cycle 24.

It is interesting to compare the daily average fluxes of $E = 2.0$ MeV electrons at $L = 4.5$ presented in this study with the upper limit of the $E = 2.0$ MeV electron flux determined from the spin-averaged electron flux data from the Energetic Particle Composition and Thermal Plasma suite aboard the Van Allen probes. On first inspection, the upper limit of the Van Allen probe spin-averaged $E = 2.0$ MeV electron flux at $L = 4.5$ (Hua et al., 2022) compares favorably with the associated 1 in 100 year event flux level (Meredith et al., 2023), but our observations (Figure 5) show that the 1 in 100 year flux level was not approached during the period 2013–2018. This highlights the difficulty when trying to accurately compare the omni-directional fluxes from BDD-IIR with the spin-averaged fluxes from the Van Allen probes with differences being expected primarily due to the different nature of the data products and the different averaging times. However, our observations can be used to put the Van Allen probe measurements into the larger context. For example, the largest daily average flux of $E = 2.0$ MeV electrons at $L = 4.5$ observed by BDD-IIR on NS41 during 2013–2018 was 1.29×10^6 cm^{-2}s^{-1}sr^{-1} on 10 October 2015 (Table 1). This flux level was surpassed during 8 relativistic electron flux events between 2003 and 2011 (Table 1 and Figure 5), showing that the upper limit of the $E = 2.0$ MeV electron fluxes at $L = 4.5$, determined from the spin-averaged flux data from the Van Allen probe measurements, can be exceeded when a longer time interval is considered. We can use our observations and extreme value analysis (Meredith et al., 2023) to estimate the limiting flux of the spin-averaged observations. The limiting daily average flux of 2.0 MeV electrons at $L = 4.5$ is 2.2×10^6 cm^{-2}s^{-1}sr^{-1} (Meredith et al., 2023), which is a factor of 1.7 larger than the maximum daily average flux of $E = 2.0$ MeV electrons at $L = 4.5$ observed by BDD-IIR during the period 2013–2018. The maximum flux spin-averaged $E = 2.0$ MeV electron flux determined from the Van Allen probe data was $\sim 2.0 \times 10^6$ cm^{-2}s^{-1}sr^{-1} (Hua et al., 2022). Assuming a similar ratio between the limiting flux and the maximum flux observed by the Van Allen probes, suggests that the limiting spin-averaged flux would be of the order 3.4×10^6 cm^{-2}s^{-1}sr^{-1}.

The largest geomagnetic storm in recorded history was the so-called Carrington storm of 1859, named after one of the first witnesses to observe and document the storm (Carrington, 1859). The magnitude of this storm has been estimated to be between -850 nT (Siscoe et al., 2006) and $-1,760$ nT (Tsurutani et al., 2003), corresponding to a factor of between 2.2 and 4.6 times larger than the Halloween storm. Simulations suggest that such a storm would result in a new belt at low L, in the inner belt, and have little effect on the fluxes in GPS orbit (Shprits et al., 2011).

Modeling work shows that satellites at geosynchronous orbit are likely to be more at risk from a fast solar wind stream event lasting more than 5 days than they are from a Carrington type event (Horne et al., 2018). The research here shows that high speed solar wind streams can produce large fluxes of relativistic electrons in GPS orbit, causing 30 and 37 of the largest fifty $E = 2.0$ MeV electron flux events at $L = 4.5$ and 6.5 respectively, primarily during the declining phase of the solar cycle. These observations are consistent with earlier studies showing that high fluxes of relativistic electrons are predominantly associated with high speed solar wind streams (e.g., Blake et al., 1997; Borovsky & Denton, 2006; Iles et al., 2002; Paulikas and Blake, 1976), and that they mostly occur during the declining phase of the solar cycle, when coronal holes and their associated high speed streams are most prevalent (Burlaga & Lepping, 1977; Gonzalez et al., 1999; Mursula & Zieger, 1996; Richardson et al., 2001). However, the largest fluxes in both locations were observed following *moderate* to *strong* CMEs.

The *great* geomagnetic storm of 10 May 2024 had a minimum Dst index of −412 nT, making it just slightly smaller than the largest storm in our study (Figure 2). Consistent with our findings, this event was not associated with a strong relativistic electron response at GEO or MEO. For example, the fluxes of $E > 2.0$ MeV electrons observed by GOES 16 were very low before the storm and remained low following the storm. In the seven day period following the storm, the highest flux of $E > 2.0$ MeV electrons observed by GOES 16 was of the order of 1,000 cm^{-2}s^{-1}sr^{-1} (https://lasp.colorado.edu/space-weather-portal/goes-electron-flux) a factor of more than 50 below the 1 in 10 year daily average flux of $E > 2$ MeV electrons at GOES East (Meredith et al., 2015). Furthermore, the quick look HEP-H instrument on board Arase (https://ergsc.isee.nagoya-u.ac.jp/data_info/erg.shtml.en) that the flux of ~2.0 MeV electrons peaked well inside MEO and was not significantly enhanced at MEO.

The $E = 2.0$ MeV fluxes at $L = 4.5$ presented in this paper are close to the knee in the electron spectra at L* = 4.25 presented in Olifer et al. (2022). This knee separates the lower energy measurements which tend to energy dependent flux limits as defined by Kennel and Petschek theory (Kennel & Petschek, 1966), with those at higher energies which lie below the Kennel and Petschek limit. Extreme value analysis (Meredith et al., 2023) reveals a similar structure with a knee in the energy spectra at $L = 4.5$ which occurs at energies between 2.0 and 3.0 MeV. Furthermore, the analysis showed that the daily averaged $E = 2.0$ MeV electron fluxes in the range 0.6–2.0 MeV at $L = 4.5$ tended to a limiting value while the higher energies were potentially unbounded. This is consistent with the analysis presented in Olifer et al. (2022) who show, using Kennel and Petschek theory applied to the Van Allen probe measurements, that there is an energy dependent flux limit for energies below 2.6 MeV.

The characteristic widths of the largest flux events are location dependent being longer at lower L, with a mean of 7.9 ± 2.5 days and 2.8 ± 1.0 days at $L = 4.5$ and 6.5 respectively. This is probably due to a combination of factors including shorter loss timescales at higher L (e.g., Claudepierre et al., 2020) and more variability at higher L due to more frequent losses to the magnetopause. This finding is relevant to satellite operators as it demonstrates that once the fluxes become elevated they are likely to remain elevated for longer near the heart of the outer radiation belt at MEO compared to GEO.

6. Conclusions

We have analyzed approximately 20 years of data from the US GPS satellite NS41 to determine the strength and type of the geomagnetic storms associated with the 50 largest $E = 2.0$ MeV electron events at $L = 4.5$ and $L = 6.5$. Our principle results are as follows.

- The 1 in 10 year flux levels were exceeded 3 times at $L = 4.5$ and 2 times at $L = 6.5$. These events were associated with *moderate* or *strong* CME-driven storms.
- Although the largest flux events were associated with *moderate* or *strong* CME-driven storms, the majority of the 50 largest flux events at $L = 4.5$ (30 out of 50) and $L = 6.5$ (37 out of 50) were associated with high speed streams.
- Both CME and HSS-driven storms are very important for relativistic electron flux enhancements in GPS orbit.
- The 1 in 3 year flux level was not exceeded following any of the top 15 geomagnetic storms as monitored by the *Dst* index.

Our results show that the largest flux enhancements in GPS-orbit are associated with *moderate* to *strong* CME-driven storms. In contrast, the largest geomagnetic storms, most often associated with extreme space weather, do not lead to significantly larger relativistic electron flux events in GPS orbit.

Appendix A: The Fifty Largest Events at $L = 4.50$

The fifty largest $E = 2.0$ MeV relativistic electron flux events at $L = 4.5$ are tabulated in Table A1. For each event, the table includes the position of the event in the top fifty, the date of the event, the Dst minimum and the date of the Dst minimum of the associated geomagnetic storm, the flux, the full width half maximum of the duration of the event and the solar driver.

Table A1

No.	Date	Dst_{min} (nT)	Flux $\left(\mathrm{cm}^{-2}\mathrm{s}^{-1}\mathrm{sr}^{-1}\mathrm{MeV}^{-1}\right)$	FWHM (days)	Driver
1	08 Apr 2010	−81 nT on 06 Apr	1.98×10^6	5.50	CME
2	14 Sep 2005	−139 nT on 11 Sep	1.93×10^6	4.89	CME
3	20 Jan 2005	−103 nT on 18 Jan	1.87×10^6	2.79	CME
4	21 Sep 2003	−65 nT on 17 Sep	1.72×10^6	5.97	HSS
5	24 Jul 2004	−99 nT on 23 Jul	1.51×10^6	8.74	CME
6	19 May 2005	−247 nT on 15 May	1.45×10^6	3.54	CME
7	18 Apr 2006	−98 nT on 14 Apr	1.45×10^6	7.55	CME
8	18 Nov 2003	−62 nT on 11 Nov	1.32×10^6	8.18	HSS
9	10 Oct 2015	−130 nT on 07 Oct	1.29×10^6	9.02	HSS
10	18 Jul 2012	−139 nT on 15 Jul	1.28×10^6	6.19	CME
11	11 Nov 2004	−374 nT on 08 Nov	1.25×10^6	8.91	CME
12	25 Apr 2017	−51 nT on 22 Apr	1.25×10^6	13.95	HSS
13	04 Aug 2003	−57 nT on 27 Jul	1.24×10^6	5.87	HSS
14	28 Oct 2016	−65 nT on 25 Oct	1.24×10^6	5.81	HSS
15	17 Dec 2006	−162 nT on 15 Dec	1.24×10^6	10.54	CME
16	30 Sep 2016	−65 nT on 29 Sep	1.23×10^6	9.00	HSS
17	24 Aug 2003	−60 nT on 22 Aug	1.18×10^6	7.97	HSS
18	18 Oct 2003	−77 nT on 15 Oct	1.12×10^6	8.30	HSS
19	11 May 2016	−95 nT on 08 May	1.08×10^6	6.23	HSS
20	16 Dec 2003	−53 nT on 09 Dec	1.08×10^6	10.08	HSS
21	05 Sep 2016	−59 nT on 02 Sep	1.04×10^6	10.09	HSS
22	12 Nov 2015	−56 nT on 10 Nov	1.03×10^6	10.25	HSS
23	21 Mar 2015	−234 nT on 17 Mar	1.03×10^6	7.45	CME
24	16 Oct 2017	−53 nT on 14 Oct	1.02×10^6	6.59	HSS
25	01 Apr 2003	−78 nT on 31 Mar	9.95×10^5	7.18	HSS
26	14 Jun 2005	−106 nT on 13 Jun	9.95×10^5	3.96	CME
27	03 Sep 2019	−52 nT on 01 Sep	9.93×10^5	7.49	HSS
28	18 Aug 2015	−98 nT on 16 Aug	9.19×10^5	6.17	CME
29	11 Mar 2005	−54 nT on 07 Mar	9.09×10^5	6.39	HSS
30	16 May 2003	−84 nT on 10 May	8.90×10^5	10.00*	CME
31	20 Jul 2017	−72 nT on 16 Jul	8.85×10^5	5.14	CME
32	13 Mar 2004	−78 nT on 11 Mar	8.62×10^5	9.58	HSS
33	13 Jul 2005	−92 nT on 10 Jul	8.61×10^5	5.70	CME
34	15 Oct 2012	−109 nT on 13 Oct	8.47×10^5	11.66	CME
35	19 Sep 2017	−33 nT on 14 Sep	8.28×10^5	10.90	HSS
36	02 Apr 2017	−70 nT on 27 Mar	8.08×10^5	6.71	HSS
37	27 Apr 2012	−120 nT on 24 Apr	8.01×10^5	7.65	CME
38	19 Mar 2003	−60 nT on 16 Mar	7.97×10^5	9.60	HSS

Table A1
Continued

No.	Date	Dst_{min}(nT)	Flux $\left(\text{cm}^{-2}\text{s}^{-1}\text{sr}^{-1}\text{MeV}^{-1}\right)$	FWHM (days)	Driver
39	06 Oct 2002	−176 nT on 01 Oct	7.94×10^5	9.16	CME
40	12 Nov 2017	−73 nT on 08 Nov	7.88×10^5	6.94	HSS
41	09 May 2003	−39 nT on 07 May	7.43×10^5	4.00*	HSS
42	25 Aug 2017	−35 nT on 19 Aug	7.03×10^5	9.36	HSS
43	26 Apr 2003	−52 nT on 24 Apr	6.88×10^5	6.00*	HSS
44	16 Feb 2004	−93 nT on 11 Feb	6.77×10^5	8.47	HSS
45	21 Feb 2016	−65 nT on 16 Feb	6.68×10^5	10.35	HSS
46	01 Oct 2017	−56 nT on 28 Sep	6.57×10^5	10.07	HSS
47	26 Jan 2004	−130 nT on 22 Jan	6.42×10^5	8.55	CME
48	07 Mar 2017	−61 nT on 01 Mar	6.38×10^5	15.27	HSS
49	10 Sep 2015	−105 nT on 09 Sep	6.36×10^5	8.48	CME
50	03 Apr 2008	−56 nT on 27 Mar	6.33×10^5	7.72	HSS

Appendix B: The Fifty Largest Events at $L = 6.50$

The fifty largest $E = 2.0$ MeV relativistic electron flux events at $L = 6.5$ are tabulated in Table B1. For each event, the table includes the position of the event in the top fifty, the date of the event, the Dst minimum and the date of the Dst minimum of the associated geomagnetic storm, the flux, the full width half maximum of the duration of the event, and the solar driver.

Table B1

No.	Date	Dst_{min}(nT)	Flux $\left(\text{cm}^{-2}\text{s}^{-1}\text{sr}^{-1}\text{MeV}^{-1}\right)$	FWHM (days)	Driver
1	10 Apr 2010	−81 nT on 06 Apr	1.45×10^5	1.92	CME
2	30 Jul 2004	−170 nT on 27 Jul	1.21×10^5	2.13	CME
3	03 Apr 2008	−56 nT on 27 Mar	7.20×10^4	4.79	HSS
4	05 Aug 2003	−57 nT on 27 Jul	6.73×10^4	1.70	HSS
5	18 Oct 2017	−53 nT on 14 Oct	6.48×10^4	2.44	HSS
6	12 May 2016	−95 nT on 08 May	6.43×10^4	1.90	HSS
7	30 Aug 2018	−175 nT on 26 Aug	6.02×10^4	3.38	CME
8	18 Dec 2003	−54 nT on 08 Dec	5.61×10^4	2.88	HSS
9	09 Apr 2005	−70 nT on 05 Apr	5.57×10^4	2.12	HSS
10	15 Nov 2004	−374 nT on 08 Nov	5.54×10^4	1.60	CME
11	19 Apr 2006	−98 nT on 14 Apr	5.47×10^4	4.35	CME
12	21 Sep 2005	−80 nT on 11 Sep	5.39×10^4	4.01	CME
13	31 May 2007	−58 nT on 23 May	5.36×10^4	3.68	HSS
14	12 Mar 2005	−54 nT on 07 Mar	5.01×10^4	2.50	HSS
15	21 Oct 2016	−109 nT on 13 Oct	4.87×10^4	3.06	CME
16	19 Jul 2012	−139 nT on 15 Jul	4.84×10^4	1.74	CME
17	08 Apr 2007	−63 nT on 01 Apr	4.79×10^4	3.56	HSS
18	28 Sep 2003	−59 nT on 24 Sep	4.71×10^4	2.72	HSS
19	19 May 2005	−247 nT on 15 May	4.60×10^4	1.57	CME
20	27 Dec 2006	−51 nT on 20 Dec	4.21×10^4	5.25	HSS

Table B1
Continued

No.	Date	Dst_{min}(nT)	Flux $(\mathrm{cm^{-2}s^{-1}sr^{-1}MeV^{-1}})$	FWHM (days)	Driver
21	27 Apr 2017	−51 nT on 22 Apr	4.20×10^4	3.18	HSS
22	24 Mar 2006	−48 nT on 19 Mar	4.16×10^4	1.75	HSS
23	17 Dec 2006	−162 nT on 15 Dec	4.04×10^4	2.53	CME
24	17 Apr 2005	−62 nT on 12 Apr	3.99×10^4	1.72	HSS
25	04 Mar 2008	−52 nT on 28 Feb	3.91×10^4	2.50	HSS
26	13 Feb 2005	−57 nT on 07 Feb	3.89×10^4	1.96	HSS
27	03 Apr 2017	−70 nT on 27 Mar	3.74×10^4	2.49	HSS
28	04 Sep 2019	−52 nT on 01 Sep	3.62×10^4	2.36	HSS
29	19 Oct 2006	−55 nT on 13 Oct	3.60×10^4	3.08	HSS
30	13 Nov 2017	−73 nT on 08 Nov	3.56×10^4	2.15	HSS
31	18 Feb 2004	−93 nT on 11 Feb	3.52×10^4	2.47	HSS
32	13 Jun 2006	−42 nT on 06 Jun	3.45×10^4	3.70	HSS
33	20 Oct 2012	−90 nT on 13 Oct	3.43×10^4	6.50	CME
34	21 Mar 2012	−88 nT on 15 Mar	3.42×10^4	3.08	CME
35	21 Feb 2016	−65 nT on 16 Feb	3.36×10^4	1.92	HSS
36	25 Mar 2003	−60 nT on 16 Mar	3.31×10^4	2.00	HSS
37	17 Oct 2004	−49 nT on 13 Oct	3.27×10^4	2.55	HSS
38	21 Sep 2017	−33 nT on 14 Sep	3.20×10^4	3.58	HSS
39	15 Apr 2008	−33 nT on 06 Apr	3.14×10^4	2.57	HSS
40	22 Sep 2006	−34 nT on 18 Sep	3.09×10^4	2.70	HSS
41	13 Nov 2015	−56 nT on 10 Nov	3.02×10^4	2.49	HSS
42	04 Jun 2011	−35 nT on 02 Jun	3.01×10^4	2.88	HSS
43	25 Jan 2007	−31 nT on 15 Jan	2.99×10^4	4.86	HSS
44	19 Jul 2017	−72 nT on 16 Jul	2.99×10^4	2.31	CME
45	02 Oct 2007	−40 nT on 29 Sep	2.85×10^4	2.31	HSS
46	16 May 2006	−28 nT on 12 May	2.84×10^4	2.63	HSS
47	10 Jun 2012	−49 nT on 3 Jun	2.81×10^4	2.41	HSS
48	26 May 2017	−39 nT on 20 May	2.81×10^4	3.50	HSS
49	06 Mar 2011	−88 nT on 01 Mar	2.80×10^4	1.83	HSS
50	06 May 2005	−40 nT on 30 Apr	2.79×10^4	1.70	HSS

Appendix C: The Fifteen Largest Storms

The peak $E = 2.0$ MeV relativistic electron fluxes at $L = 4.5$ and $L = 6.5$ associated with the fifteen largest geomagnetic storms are tabulated in Table C1. For each storm, the table includes the position of the storm in the top fifteen, the date of the storm, the associated Dst minimum, the date of the associated peak flux and the peak flux at $L = 4.5$ and the date of the associated peak flux and the peak flux at $L = 6.5$.

Table C1

No.	Storm date	Dst_{min}(nT)	L = 4.5 Date	L = 4.5 Peak flux $(cm^{-2}s^{-1}sr^{-1}MeV^{-1})$	L = 6.5 Date	L = 6.5 Peak flux $(cm^{-2}s^{-1}sr^{-1}MeV^{-1})$
1	20 Nov 2003	−422	26 Nov	2.41×10^5	27 Nov	1.26×10^4
2	31 Mar 2001	−387	04 Apr	2.33×10^5	02 Apr	3.20×10^1
3	30 Oct 2003	−383	03 Nov	3.63×10^5	03 Nov	4.65×10^3
4	08 Nov 2004	−374	11 Nov	1.25×10^6	15 Nov	5.53×10^4
5	06 Nov 2001	−292	12 Nov	1.25×10^5	13 Nov	2.40×10^3
6	11 Apr 2001	−271	17 Apr	2.05×10^5	15 Apr	3.20×10^3
7	15 May 2005	−247	19 May	1.45×10^6	19 May	4.60×10^4
8	17 Mar 2015	−234	21 Mar	1.03×10^6	22 Mar	1.28×10^4
9	24 Nov 2001	−221	02 Dec	7.23×10^3	30 Nov	3.60×10^1
10	23 Jun 2015	−198	25 Jun	4.79×10^5	03 Jul	2.45×10^4
11	21 Oct 2001	−187	27 Oct	2.11×10^4	25 Oct	1.19×10^2
12	08 Sep 2002	−181	14 Sep	3.11×10^5	15 Sep	4.53×10^3
13	01 Oct 2002	−176	06 Oct	7.94×10^5	06 Oct	1.63×10^3
14	26 Aug 2018	−175	28 Aug	6.31×10^5	30 Aug	6.02×10^4
15	20 Dec 2015	−166	22 Dec	3.81×10^5	26 Dec	3.33×10^3

Data Availability Statement

The data used in this study is publicly available from http://www.ngdc.noaa.gov/stp/space-weather/satellite-data/satellite-systems/gps/data/ns41. The solar wind data, geomagnetic activity indices and sunspot numbers are available from the NASA GSFC OMNI website (https://omniweb.gsfc.nasa.gov/). The results and data shown in this study can be downloaded from the UK Polar Data Centre at Meredith et al. (2024).

References

Baker, D. N., Blake, J. B., Callis, L. B., Cummings, J. R., Hovestadt, D., Kanekal, S., et al. (1994). Relativistic electron acceleration and decay time scales in the inner and outer radiation belts: Sampex. *Geophysical Research Letters*, *21*(6), 409–412. https://doi.org/10.1029/93GL03532

Baker, D. N., Kanekal, S. G., Horne, R. B., Meredith, N. P., & Glauert, S. A. (2007). Low-altitude measurements of 2–6 MeV electron trapping lifetimes at $1.5 \leq L \leq 2.5$. *Geophysical Research Letters*, *34*(20), L20110. https://doi.org/10.1029/2007GL031007

Baker, D. N., Kanekal, S. G., Li, X., Monk, S. P., Goldstein, J., & Burch, J. L. (2004). An extreme distortion of the Van Allen belt arising from the "Hallowe'en" solar storm in 2003. *Nature*, *432*(7019), 878–881. https://doi.org/10.1038/nature03116

Blake, J. B., Baker, D. N., Turner, N., Ogilvie, K. W., & Lepping, R. P. (1997). Correlation of changes in the outer-zone relativistic electron population with upstream solar wind and magnetic field measurements. *Geophysical Research Letters*, *24*(8), 927–929. https://doi.org/10.1029/97GL00859

Blake, J. B., Kolasinski, W. A., Fillius, R. W., & Mullen, E. G. (1992). Injection of electrons and protons with energies of tens of MeV into L \lessbin 3 on 24 March 1991. *Geophysical Research Letters*, *19*(8), 821–824. https://doi.org/10.1029/92GL00624

Borovsky, J. E., & Denton, M. H. (2006). Differences between CME-driven storms and CIR-driven storms. *Journal of Geophysical Research*, *111*(A7), A07S08. https://doi.org/10.1029/2005JA011447

Burlaga, L. F., & Lepping, R. P. (1977). The causes of recurrent geomagnetic storms. *Planetary and Space Science*, *25*(12), 1151–1160. https://doi.org/10.1016/0032-0633(77)90090-3

Cabinet Office. (2012). National risk register of Civil Emergencies. Cabinet Office, 70 Whitehall, London. [Retrieved from www.cabinetoffice.gov.uk

Cabinet Office. (2018). Public summary of sector security and resilience plans. Cabinet Office, 70 Whitehall, London. [Retrieved from www.cabinetoffice.gov.uk

Cabinet Office. (2023). National risk register of Civil Emergencies. Cabinet Office, 70 Whitehall, London. [Retrieved from www.cabinetoffice.gov.uk

Carrington, R. C. (1859). Description of a singular appearance seen in the Sun on September 1, 1859. *Monthly Notices of the Royal Astronomical Society*, *20*(1), 13–15. https://doi.org/10.1093/mnras/20.1.13

Cayton, T. E., Belian, R. D., Gary, S. P., Fritz, T. A., & Baker, D. N. (1989). Energetic electron components at geosynchronous orbit. *Geophysical Research Letters*, *16*(2), 147–150. https://doi.org/10.1029/GL016i002p00147

Cayton, T. E., Chen, Y., Friedel, R. H. W., & Kippen, R. M. (2010). *Analysis of electron and proton environmental data for medium-earth orbit (2000-present)*. Technical Report LA-UR-10-04234. National Laboratory.

Cayton, T. E., Drake, D. M., Spencer, K. M., Herrin, M., Wehner, T. J., & Reedy, R. C. (1998). *Description of the BDD-IIR: Electron and proton sensors on the GPS*. Los Alamos National Laboratory.

Claudepierre, S. G., Ma, Q., Bortnik, J., O'Brien, T. P., Fennell, J. F., & Blake, J. B. (2020). Empirically estimated electron lifetimes in the Earth's radiation belts: Comparison with theory. *Geophysical Research Letters*, *47*(3). https://doi.org/10.1029/2019GL086056

Cranmer, S. R. (2009). Coronal holes. *Living Reviews in Solar Physics*, *6*, 366. https://doi.org/10.12942/lrsp-2009-3

Denton, M. H., & Borovsky, J. E. (2012). Magnetosphere response to high-speed solar wind streams: A comparison of weak and strong driving and the importance of extended periods of fast solar wind. *Journal of Geophysical Research*, *117*(A9), A00L05. https://doi.org/10.1029/2011JA017124

Denton, M. H., Borovsky, J. E., Skoug, R. M., Thomsen, M. F., Lavraud, B., Henderson, M. G., et al. (2006). Geomagnetic storms driven by ICME- and CIR-dominated solar wind. *Journal of Geophysical Research*, *111*(A7), A07S07. https://doi.org/10.1029/2005JA011436

Duderstadt, J. J., & Hamilton, L. J. (1976). *Nuclear reactor analysis* (pp. 381–383). John Wiley.

Frederickson, A. R., Mullen, E. G., Brautigam, D. H., Kerns, K. J., & Holman, E. G. (1991). Radiation induced insulator discharge pulses in the CRRES internal discharge monitor satellite experiment. *IEEE Transactions on Nuclear Science*, *38*(6), 778–784. https://doi.org/10.1109/23.124153

Gabrielse, C., Lee, J. H., Claudepierre, S., Walker, D., O'Brien, P., Roeder, J., et al. (2022). Radiation Belt Daily Average Electron flux model (RB-Daily-E) from the seven-year Van Allen Probes mission and its application to interpret GPS on-orbit solar array degradation. *Space Weather*, *20*(11), e2022SW003183. https://doi.org/10.1029/2022SW003183

Gonzalez, W. D., Tsurutani, B. T., & Clua de Gonzalez, A. L. (1999). Interplanetary origin of geomagnetic storms. *Space Science Reviews*, *88*(3/4), 529–562. https://doi.org/10.1023/A:1005160129098

Gopalswamy, N., & Kundu, M. R. (1992). Estimation of the mass of a coronal mass ejection from radio observations. *The Astrophysical Journal*, *390*, L37–L39. https://doi.org/10.1086/186366

Grandin, M., Aikio, A. T., & Kozlovsky, A. (2019). Properties and geoeffectiveness of solar wind high-speed streams and stream interaction regions during solar cycles 23 and 24. *Journal of Geophysical Research: Space Physics*, *124*(6), 3871–3892. https://doi.org/10.1029/2018JA026396

Horne, R. B., Phillips, M. W., Glauert, S. A., Meredith, N. P., Hands, A. D. P., Ryden, K., & Li, W. (2018). Realistic worst case for a severe space weather event driven by a fast solar wind stream. *Space Weather*, *16*(9), 1202–1215. https://doi.org/10.1029/2018SW001948

Horne, R. B., Thorne, R. M., Shprits, Y. Y., Meredith, N. P., Glauert, S. A., Smith, A. J., et al. (2005). Wave acceleration of electrons in the Van Allen radiation belts. *Nature*, *437*(7056), 227–230. https://doi.org/10.1038/nature03939

Hua, M., Bortnik, J., & Ma, Q. (2022). Upper limit of outer radiation belt electron acceleration driven by whistler-mode chorus waves. *Geophysical Research Letters*, *49*(15), e2022GL099618. https://doi.org/10.1029/2022GL099618

Iles, R. H. A., Fazakerley, A. N., Johnstone, A. D., Meredith, N. P., & Bühler, P. (2002). The relativistic electron response in the outer radiation belt during magnetic storms. *Annales Geophysicae*, *20*(7), 957–965. https://doi.org/10.5194/angeo-20-957-2002

Jaynes, A. N., Baker, D. N., Singer, H. J., Rodriguez, J. V., Loto'aniu, T. M., Ali, A. F., et al. (2015). Source and seed populations for relativistic electrons: Their roles in radiation belt changes. *Journal of Geophysical Research: Space Physics*, *120*(9), 7240–7254. https://doi.org/10.1002/2015JA021234

Kennel, C. F., & Petschek, H. E. (1966). Limit on stably trapped particle fluxes. *Journal of Geophysical Research*, *71*(1), 1–28. https://doi.org/10.1029/JZ071i001p00001

Kilpua, E., Balogh, A., Von Steiger, R., & Liu, Y. (2017). Geoeffective properties of solar transients and stream interaction regions. *Space Science Reviews*, *212*(3), 1271–1314. https://doi.org/10.1007/s11214-017-0411-3

Koller, J., Chen, Y., Reeves, G. D., Friedel, R. H. W., Cayton, T. E., & Vrugt, J. A. (2007). Identifying the radiation belt source region by data assimilation. *Journal of Geophysical Research*, *112*(A6), A06244. https://doi.org/10.1029/2006JA012196

Koons, H. C., & Fennel, J. F. (2006). Space weather effects on communications satellites. *URSI Radio Science Bulletin*, *316*, 27–41.

Kozyra, J. U., Crowley, G., Emery, B. A., Fang, X., Maris, G., Mlynczak, M. G., et al. (2006). Response of the upper/middle atmosphere to coronal holes and powerful high-speed solar wind streams in 2003. In B. T. Tsurutani (Ed.), *Corotating solar wind streams and recurrent geomagnetic activity, geophysical monograph series* (Vol. 167, pp. 319–340). AGU. https://doi.org/10.1029/167gm24

Li, W., & Hudson, M. K. (2019). Earth's van allen radiation belts: From discovery to the van allen probes era. *Journal of Geophysical Research: Space Physics*, *124*(11), 8319–8351. https://doi.org/10.1029/2018JA025940

Li, W., Thorne, R. M., Angelopoulos, V., Bortnik, J., Cully, C. M., Ni, B., et al. (2009). Global distribution of whistler-mode chorus waves observed on the THEMIS spacecraft. *Geophysical Research Letters*, *36*(9), L09104. https://doi.org/10.1029/2009GL037595

Loewe, C. A., & Prolls, G. W. (1997). Classification and mean behaviour of magnetic storms. *Journal of Geophysical Research*, *102*, 209–214. https://doi.org/10.1029/96JA04020

Meredith, N., Cayton, T., & Cayton, M. (2024). Strong relativistic electron flux events in GPS orbit (2000 - 2020) (Version 1.0). [Dataset]. *NERC EDS UK Polar Data Centre*. https://doi.org/10.5285/dd8dee98-b75e-4b2f-a002-3f00bcc29d35

Meredith, N. P., Cain, M., Horne, R. B., Thorne, R. M., Summers, D., & Anderson, R. R. (2003). Evidence for chorus-driven electron acceleration to relativistic energies from a survey of geomagnetically disturbed periods. *Journal of Geophysical Research*, *108*(A6), 1248. https://doi.org/10.1029/2002JA009764

Meredith, N. P., Cayton, T. E., Cayton, M. D., & Horne, R. B. (2023). Extreme relativistic electron fluxes in GPS orbit: Analysis of NS41 BDD-IIR data. *Space Weather*, *21*(6), e2023SW003436. https://doi.org/10.1029/2023SW003436

Meredith, N. P., Horne, R. B., & Anderson, R. R. (2001). Substorm dependence of chorus amplitudes: Implications for the acceleration of electrons to relativistic energies. *Journal of Geophysical Research*, *106*(A7), 13165–13178. https://doi.org/10.1029/2000JA900156

Meredith, N. P., Horne, R. B., Isles, J. D., & Rodriguez, J. V. (2015). Extreme relativistic electron fluxes at geosynchronous orbit: Analysis of GOES $E > 2$ MeV electrons. *Space Weather*, *13*(3), 170–184. https://doi.org/10.1002/2014SW001143

Meredith, N. P., Horne, R. B., Shen, X.-C., Li, W., & Bortnik, J. (2020). Global model of whistler mode chorus in the near-equatorial region ($|\lambda_m| < 18°$). *Geophysical Research Letters*, *47*(11), e2020GL087311. https://doi.org/10.1029/2020GL087311

Messenger, S. R., Jackson, E. M., Warner, J. H., Walters, R. J., Cayton, T. E., Chen, Y., et al. (2011). Correlation of telemetered solar array data with particle detector data on GPS spacecraft. *IEEE Transactions on Nuclear Science*, *58*(6), 3118–3125. https://doi.org/10.1109/TNS.2011.2172957

Mursula, K., & Zieger, B. (1996). The 13.5-day periodicity in the sun, solar wind, and geomagnetic activity: The last three solar cycles. *Journal of Geophysical Research*, *101*(A12), 27–077. https://doi.org/10.1029/96JA02470

Olifer, L., Mann, I. R., Claudepierre, S. G., Baker, D. N., Spence, H. E., & Ozeke, L. G. (2022). A natural limit to the spectral hardness of worst case electron radiation in the terrestrial Van Allen belt. *Journal of Geophysical Research: Space Physics*, *127*(8), e2022JA030506. https://doi.org/10.1029/2022JA030506

Olson, W. P., & Pfitzer, K. (1977). Magnetospheric magnetic field modelling annual scientific report. *Air Force Office of Scientific Research*.

Paulikas, G. A., & Blake, J. B. (1979). Effects of the solar wind on magnetospheric dynamics: Energetic electrons at the synchronous orbit. In W. P. Olson (Ed.), *Quantitive modelling of magnetospheric processes, Geophysical monograph series* (Vol. 21, pp. 180–202). AGU. https://doi.org/10.1029/gm021p0180

Pierrard, V., & Lemaire, J. (1996). Fitting AE8 energy spectra with two Maxwellian functions. *Radiation Measurements*, *26*(3), 333–337. https://doi.org/10.1016/1350-4487(96)00057-1

Pultarova, T. (2023). *GPS satellites threatened more by mild solar storms than monster solar flares, space*. com. Retrieved from https://www.space.com/mild-solar-storms-threat-gps-satellites

Reagan, J. B., Nightingale, R. W., Gaines, E. E., Imhof, W. L., & Stassinopoulos, E. G. (1981). Outer zone energetic electron spectral measurements. *Journal of Spacecraft and Rockets*, *18*(1), 83–88. https://doi.org/10.2514/3.57791

Reeves, G. D., Chen, Y., Cunningham, G. S., Friedel, R. W. H., Henderson, M. G., Jordanova, V. K., et al. (2012). Dynamic radiation environment assimilation model: Dream. *Space Weather*, *10*(3), S03006. https://doi.org/10.1029/2011SW000729

Richardson, I., & Cane, H. (2024). *Near-earth interplanetary coronal mass ejections since January 1996*. *Harvard Dataverse, V2*. https://doi.org/10.7910/DVN/C2MHTH

Richardson, I. G., Cliver, E. W., & Cane, H. V. (2001). Sources of geomagnetic storms for solar minimum and maximum conditions during 1972–2000. *Geophyical Research Letters*, *28*(13), 2569–2572. https://doi.org/10.1029/2001GL013052

Richardson, I. G., Webb, D. F., Zhang, J., Berdichevsky, D. B., Biesecker, D. A., Kasper, J. C., et al. (2006). Major geomagnetic storms (Dst < −100 nT) generated by corotating interaction regions. *Journal of Geophysical Research*, *111*(A7), A07S09. https://doi.org/10.1029/2005JA011476

Rodgers, D. J., & Ryden, K. A. (2001). Internal charging in space. In R. A. Harris (Ed.), *Proceedings of 7th spacecraft charging technology conference, noordwijk, The Netherlands, 23-27 April, ESA SP-476* (p. 25). European Space Agency.

Royal Academy of Engineering Report. (2013). *Extreme space weather: Impacts on engineered systems and infrastructure*. Royal Academy of Engineering.

Sawadogo, S., Gnabahou, D. A., Pahima, T., & Ouattara, F. (2024). Solar activity: Towards a standard classification of solar phases from cycle 1 to cycle 24. *Advances in Space Research*, *73*, 1041–1049. https://doi.org/10.1016/j.asr.2023.11.011

Shi, R., Summers, D., Ni, B., Fennell, J. F., Blake, J. B., Spence, H. E., & Reeves, G. D. (2016). Survey of radiation belt energetic electron pitch angle distributions based on the Van Allen Probes MagEIS measurements. *Journal of Geophysal Research Space Physics*, *21*(2), 1078–1090. https://doi.org/10.1002/2015JA021724

Shprits, Y., Subbotin, D., Ni, B., Horne, R., Baker, D., & Cruce, P. (2011). Profound change of the near-Earth radiation environment caused by solar superstorms. *Space Weather*, *9*(8), S08007. https://doi.org/10.1029/2011SW000662

Shprits, Y. Y., Elkington, S. R., Meredith, N. P., & Subbotin, D. A. (2008). Review of modeling of losses and sources of relativistic electrons in the outer radiation belt I: Radial transport. *Journal of Atmospheric and Solar-Terrestrial Physics*, *70*(14), 1679–1693. https://doi.org/10.1016/j.jastp.2008.06.008

Shprits, Y. Y., Subbotin, D. A., Meredith, N. P., & Elkington, S. R. (2008). Review of modeling of losses and sources of relativistic electrons in the outer radiation belt II: Local acceleration and loss. *Journal of Atmospheric and Solar-Terrestrial Physics*, *70*(14), 1694–1713. https://doi.org/10.1016/j.jastp.2008.06.014

Siscoe, G., Crooker, N. U., & Clauer, C. R. (2006). Dst of the Carrington storm of 1859. *Advances in Space Research*, *38*(2), 173–179. https://doi.org/10.1016/j.asr.2005.02.102

St. Cyr, O. C., Howard, R. A., Sheeley, N. R., Jr., Plunkett, S. P., Michels, D. J., Passwaters, S. E., et al. (2000). Properties of coronal mass ejections: SOHO LASCO observations from January 1996 to June 1998. *Journal of Geophysical Research*, *105*(A8), 18169–18185. https://doi.org/10.1029/1999JA000381

Thorne, R., Li, W., Ni, B., Ma, Q., Bortnik, J., Chen, L., et al. (2013). Rapid local acceleration of relativistic radiation-belt electrons by magnetospheric chorus. *Nature*, *504*(7480), 411–414. https://doi.org/10.1038/nature12889

Thorne, R. M. (2010). Radiation belt dynamics: The importance of wave-particle interactions. *Geophysical Research Letters*, *37*(22), L22107. https://doi.org/10.1029/2010GL044990

Tsurutani, B. T., Gonzalez, W. D., Gonzalez, A. L. C., Tang, F., Arballo, J. K., & Okada, M. (1995). Interplanetary origin of geomagnetic activity in the declining phase of the solar cycle. *Journal of Geophysical Research*, *100*(A11), 21717–21733. https://doi.org/10.1029/95JA01476

Tsurutani, B. T., Gonzalez, W. D., Lakhina, G. S., & Alex, S. (2003). The extreme magnetic storm of 1-2 September 1859. *Journal of Geophysical Research*, *108*(A7), 1268. https://doi.org/10.1029/2002JA009504

Turner, N. E., Mitchell, E. J., Knipp, D. J., & Emery, B. A. (2006). Energetics of magnetic storms driven by corotating interation regions: A study of geoeffectiveness. In B. T. Tsurutani (Ed.), *Co-rotating solar wind streams and recurrent geomagnetic activity, geophysical monograph series* (Vol. 167, pp. 113–340). AGU.

Tuszewski, M., Cayton, T. E., & Ingraham, J. C. (2002). A new numerical technique to design satellite energetic electron detectors. *Nuclear Instruments and Methods in Physics Research, Section A*, *482*(3), 653–666. https://doi.org/10.1016/S0168-9002(01)01735-1

Varotsou, A., Friedel, R. H., Reeves, G. D., Lavraud, B., Skoug, R. M., Cayton, T. E., & Bourdarie, S. (2008). Characterization of relativistic electron flux rise times during the recovery phase of geomagnetic storms as measured by the NA41 GPS satellite. *Journal of Atmospheric and Solar-Terrestrial Physics*, *70*(14), 1745–1759. https://doi.org/10.1016/j.jastp.2008.01.020

Yermolaev, Y. U., & Yermolaev, M. Y. (2002). Statistical relationships between solar, interplanetary, and geomagnetospheric disturbances, 1976–2000. *Cosmic Research*, *40*, 1. https://doi.org/10.1023/B:COSM.0000007952.09069.b8